

Full paper

Formation of heterostructures via direct growth CN on *h*-BN porous nanosheets for metal-free photocatalysis

Zuoli He^a, Chuhyung Kim^a, Lihua Lin^b, Tae Hwa Jeon^a, Sen Lin^b, Xinchun Wang^{b,*}, Wonyong Choi^{a,*}

^a Division of Environmental Science and Engineering and Department of Chemical Engineering, Pohang University of Science and Technology (POSTECH), Pohang 37673, Republic of Korea

^b State Key Laboratory of Photocatalysis on Energy and Environment, College of Chemistry, Fuzhou University, Fuzhou 350-002, China



ARTICLE INFO

Keywords:

Boron nitride
Carbon nitride
Semiconductor hybrids
Photocatalysts
H₂ production

ABSTRACT

Many recent advances in creating heterostructures based on 2D materials have opened new possibilities in catalysis. This study prepared a new 2D hybrid photocatalyst (CBN-x) consisting of CN and *h*-BN using low-cost precursors (urea and boric acid). The effects of CN loading on the structure, surface chemistry and photocatalytic activities were systematically investigated. The photocatalytic activities of CBN-x samples were tested for the production of H₂ and H₂O₂, which demonstrated markedly enhanced activities without the need of noble metal co-catalysts. However, CBN-x activities for the photocatalytic oxidation of organic compound were not better than that of *h*-BN. Loading CN on *h*-BN sheets, C 2p and N 2p orbitals from CN introduce new valence and conduction band edges, which gradually narrowed the bandgap and enhanced light absorption efficiency of the hybrid photocatalysts. In such metal-free systems, electrons generated in CN transfer to *h*-BN, while photo-generated holes on *h*-BN transfer to CN, which enhances the charge separation through the heterojunction interface (CN/BN). Therefore, increasing the CN loading enhances the overall efficiency of photocatalysis until excessive loading of CN covers the active sites on *h*-BN.

1. Introduction

Graphene and other two-dimensional (2D) materials are of considerable interests in catalysis because of their unique structural and electronic properties [1–3]. Many of them are stable in ambient conditions, and their electronic properties are often very different from those of their 3D counterparts. The different electronic properties may induce different chemical reactivity and unexpected performances in some applications including catalysis [4–7]. For example, the surface properties of some 2D materials (such as C₃N₄, *h*-BN, MoS₂) can significantly affect catalytic activity and selectivity [8–13]. In particular, the 2D-materials have been widely investigated as successful photocatalysts in various applications, including organic pollutants degradation, hydrogen production, and carbon dioxide reduction [14–16]. However, their catalytic properties need to be further improved to meet requirements of practical applications. Many recent advances in creating heterostructures based on 2D materials including graphene provide new possibilities in catalysis [5,17–19]. A single-atomic layered material heterojunctioned at the surface of the other layered materials modifies the electronic state through the difference in

work function, and the formation of hybrid structures of different 2D materials enable unprecedented flexibility in controlling the chemical reactivity [20].

Hexagonal boron nitride (*h*-BN), so-called ‘white graphene’, is a representative 2D crystal with strong covalent sp² bonds in the plane and a large bandgap. It has versatile applications owing to its excellent chemical stability, good thermal stability and conductivity [11,21–24]. As *h*-BN is composed of light elements, it has high gravimetric uptake capacity. In addition, the polarity of B–N bonds and the high surface area of *h*-BN nanostructures provide large adsorption capacity for various substances [21,25,26]. Its high chemical and thermal stability also make the removal and recycling process easy. BN-based materials have good catalytic applications, which include hydrogen production [10], oxidation of organic pollutants [26,27], ammonia synthesis [28], CO₂ reduction [29], NO_x reduction or selective oxidative dehydrogenation [11]. On the other hand, polymeric CN, consisting of tri-*s*-triazine building blocks, has been successfully applied in photo- and electrocatalysis [6,30–32], and its catalytic performance can be improved by the hybridization with other 2D materials, such as graphene and its derivatives [33,34].

* Corresponding authors.

E-mail addresses: xwang@fzu.edu.cn (X. Wang), wchoi@postech.edu (W. Choi).

Herein, we investigated a new 2D heterostructure based on the hybridization of *h*-BN and CN, focusing in particular on the photocatalytic activity of the composite materials. BN possesses wide bandgaps as N 2p orbitals form a deep valence band, therefore modifying the valence band structure is one of the key strategies for the development of BN based photocatalysts. The present study demonstrates that loading CN on *h*-BN sheets exhibits outstanding photocatalytic activity for the production of H₂ and H₂O₂ compared with Pt-loaded BN. We also carried out first-principle calculations which revealed the unique physical features of CN/BN heterostructures.

2. Results and discussion

2.1. Structures and compositions of the hybrid photocatalysts

In this article, we develop a facile method using two-step calcinations for the direct growth of CN on *h*-BN nanosheets as shown in Fig. S1. Typically, white *h*-BN samples were obtained from treating boric acid and urea at 900 °C for 5 h under nitrogen gas. In the second step, we used urea as CN source. Different amounts of urea were mixed with *h*-BN by fully grinding in an agate mortar. The mixed powder was put into a 30 mL alumina crucible with a cover and heated to 550 °C in a muffle furnace for 30 min. The resulted powder was collected after washing with water to remove B₂O₃. The final samples were denoted as CBN-x, where x (1, 2, 4, 6, 8, 10) is the mass ratio of urea to BN in CN growth process. As shown in Fig. 1a, *h*-BN sample shows a main peak around 26°, attributable to the (002) planes of the graphitic *h*-BN. After post-thermal treatment with urea, all CBN-x samples featured XRD peaks similar to those of *h*-BN. The main peak increased with increasing the urea loading (CBN1 → CBN4) but further increase of urea loading reduced and broadened the peak, which could indicate the loading of CN on *h*-BN and the formation of new interfacial phases. On the other hand, the sign of CN peak was hardly seen because of its low XRD intensity, therefore, the presence of CN was confirmed by other analytical methods (vide infra), such as transmission electron microscopy (TEM), scanning electron microscope (SEM), X-ray photoelectron spectroscopy (XPS), UV–Visible absorption (UV–Vis) and Fourier transform infrared spectroscopy (FTIR). Loading CN on *h*-BN sheets enabled the fine adjustment of the optical properties as shown in the UV–Vis spectra of CBN-x samples. The absorption edge shows a clear red shift with increasing the urea loading (see Fig. 1b), indicating a decrease of the bandgap with increasing CN loading on the *h*-BN nanosheets. The determined bandgaps of these CBN-x samples are listed in Table 1. The porous structure and surface area of CBN-x samples were investigated by N₂-adsorption measurements. The N₂ adsorption–desorption isotherms (Fig. 1c) of *h*-BN, CBN-6, and CBN-8 are characteristic of type-IV with a hysteresis loop, demonstrating the presence of highly porous texture. The corresponding BJH pore size distributions (inset in Fig. 1c) derived from the adsorption isotherms show a minor difference between *h*-BN and CBN-x samples. The BET surface areas and average pore size of CN and CBN-x samples are compared in Table 1. The BET surface areas and average pore sizes of CBN-x samples decreased with increasing the CN loading.

The morphology and crystallography of the samples were examined using a field-emission scanning electron microscope (FE-SEM; JEOL, JSM-7401F) and a high-resolution transmission electron microscope (HR-TEM; JEOL, JEM-2200FS) with the electron energy-loss spectroscopy (EELS) analysis. Detailed TEM images revealed the presence of nanosheets with pores in both *h*-BN and CBN-6 samples. Fig. 2 shows that pores with the diameter about 20 nm are present across the *h*-BN sheets, which is consistent with the porosity and surface area measurements shown in Table 1. The microstructure of the porous *h*-BN sheet was further investigated by HR-TEM. The HR-TEM image (Fig. 2c–d) showed the porous nanosheets were composed of 3–5 stacked layers and have about 5 nm thickness. During the synthesis process, the decomposition of boric acid and urea released gaseous

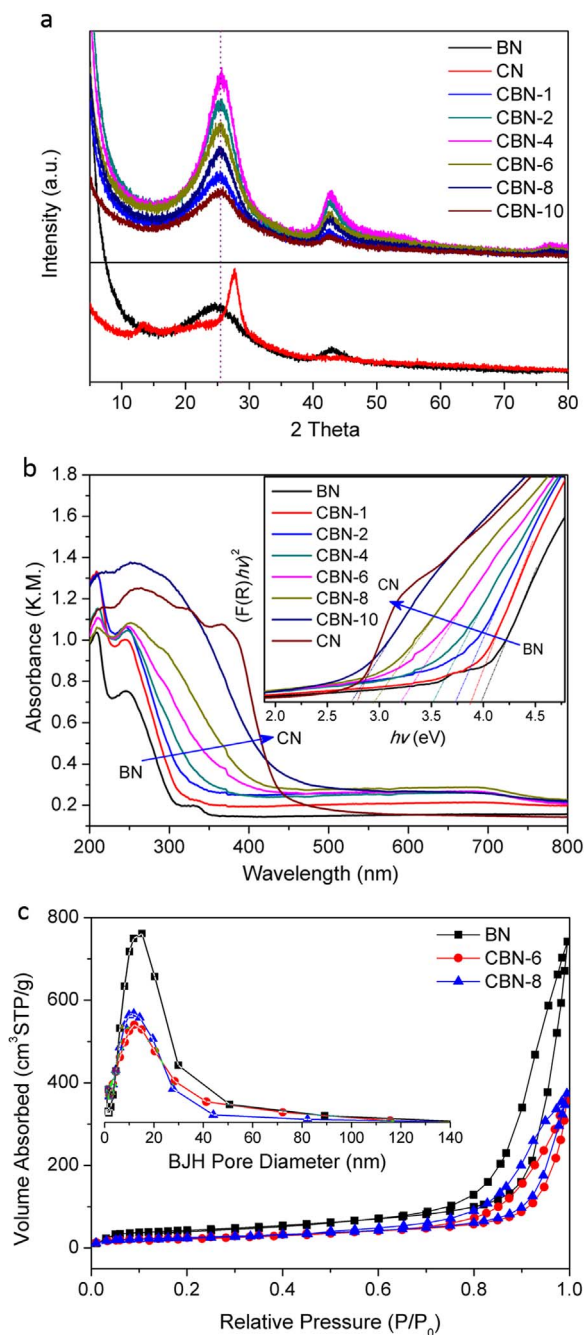


Fig. 1. (a) XRD patterns of BN, CN and CBN-x samples. (b) Diffuse reflectance spectra and the estimated bandgap energies of *h*-BN and CBN-x samples. (c) N₂-sorption isotherms and corresponding pore size distribution plots (inset).

products like NH₃, N₂, and CO, which might create bubbles and suppress the growth of *h*-BN in this regions with leaving the porous structure [25]. Fig. 2e–f show that CBN-6 was composed of 4–6 stacked layers and also retained the porous structure even after CN was loaded on *h*-BN nanosheets. Both *h*-BN and CN have similar stacking van der Waals interactions with exhibiting a similar interplane distance [35], which should facilitate the loading of CN layers on the *h*-BN surface along (002) planes. HR-TEM image (see Fig. 2h) revealed the layered CN structure was formed on *h*-BN surface. Element mapping of CBN-6 showed a uniform distribution of B, C, and N throughout the whole selected area whereas *h*-BN exhibited B and N only with a negligible presence of C. The SEM images also show that both *h*-BN and CBN-1/CBN-6 samples revealed a porous bulk network composed of nanosheets (see Fig. S2).

Table 1
Effects of CN content on the physical-chemical properties and photocatalytic activities of the CBN-x samples.

Samples	Details in experiments		H ₂ production (μmol/h)	H ₂ O ₂ formation (μmol/min)	H ₂ O ₂ decomposition (μmol/min)	Surface chemical composition					BET surface area (m ² /g)	Average pore size (nm)	Band gap (eV)
	BN (g)	Urea (g)				B at%	C at%	N at%	O at%	CN at%			
BN	–	–	0.8	19.1	14.2	42.4	4.0	39.5	14.1	0	236	20.7	3.95
CBN-1	0.2	0.2	0.7	15.3	11.0	40.0	5.0	41.6	13.4	2.2	180	20.4	3.84
CBN-2	0.2	0.4	1.5	22.1	9.4	38.1	7.7	44.1	10.1	8.9	93	19.4	3.68
CBN-4	0.2	0.8	1.7	29.5	7.7	36.3	9.5	43.6	10.6	13.2	87	16.0	3.47
CBN-6	0.2	1.2	2.4	50.2	7.1	30.2	14.7	43.8	11.3	26.2	86	15.5	3.13
CBN-8	0.2	1.6	1.5	59.8	6.8	23.6	20.5	43.8	12.1	41.1	84	15.0	2.86
CBN-10	0.2	2.0	0.3	24.7	5.3	15.4	28.1	43.6	12.9	61.0	79	14.5	2.67
CN	–	2	0.1	44.4	4.0	–	34.8	55.4	9.8	–	86	15.8	2.76

We characterized the surface compositions and valence states of *h*-BN and CBN-x samples, as shown in Fig. 3. XPS survey spectra of these samples revealed that they consisted of B, C, N and O elements only. The intensity of C1s peak increased with increasing urea loading, which means that higher carbon content was loaded on *h*-BN. For the *h*-BN nanosheets, B1s and N1s spectra showed main binding energies of 190.7 eV and 398.2 eV, respectively. The shoulder peak at 192.2 eV in the B1s spectrum is assigned to B–O bonds, which can be related with the bridge B–O–B in the *h*-BN network. The high resolution C1s and N1s spectra of CBN-x samples show both N–C=N peak located at 288.40 eV and C–N=C peak located around 399.45 eV, which suggests the formation of CN on the surface [35]. The intensity of these peaks increased with urea loading, indicating a higher content of CN loaded on BN. In particular, it should be noted that B–N–C peak was also found in N 1s spectra. The quantitative composition analysis of B, N and C elements in the CBN-x samples was present in Table 1. In order to address the rough CN ratio on the photocatalyst surface, we assumed that a) the content of adsorbed C species was the same in all the samples; b) other C species was all from CN; c) all B was from BN. The rough CN contents estimated based on these assumptions are 2.2, 8.9, 13.2, 26.2, 41.1, 61.0% for CBN-x (1, 2, 4, 6, 8, 10), respectively. The peak at 531.4 eV in O 1s spectra of CBN-x samples is attributed to surface OH (O_{OH}) species (see Fig. S3). The FTIR spectra of *h*-BN and CBN-x samples show intense absorptions at 1375 and 787 cm⁻¹, ascribed to the characteristic stretching (ν_{B–N}) and bending mode (δ_{B–N}) of sp²-hybridized *h*-BN skeleton, respectively (see Fig. S4). The peaks at 1200–1600 cm⁻¹ region

in pure CN spectrum are assigned to the stretching modes of C–N heterocycles. A new absorption peak around 1600 cm⁻¹ was found in the CBN-x samples, which also supports that CN was formed on the *h*-BN surface.

2.2. Photocatalytic properties of the hybrid photocatalysts

The photocatalytic activity tests were carried out in aqueous suspension using two different methods: (1) H₂ production from H₂O reduction and (2) H₂O₂ production from O₂ reduction in the presence of methanol as a hole-scavenger.

2.2.1. Photocatalytic H₂ production

The as-prepared *h*-BN and CBN-x samples exhibited a steady production of H₂ from methanol solution under light illumination (λ > 305 nm) in the absence of noble metal co-catalysts such as Pt, Au, and Ag, whereas pure CN showed negligible activity for H₂ production. Fig. 4a shows the effect of CN content in CBN-x samples on photocatalytic H₂ production. It should be noted that *h*-BN phase has an intrinsic catalytic activity for H₂ production. The photocatalytic activity of H₂ production increased with increasing the urea loading and optimized at CBN-6. Further increasing the urea amount decreased the photocatalytic activity probably because of the light-shielding effect of the CN layer deposited on *h*-BN sheets. As confirmed by XPS data (see Fig. 3), the CN layer was formed when the mass ratio of urea to BN was as low as 2 (CBN-2). As illustrated in the band position diagram of *h*-BN

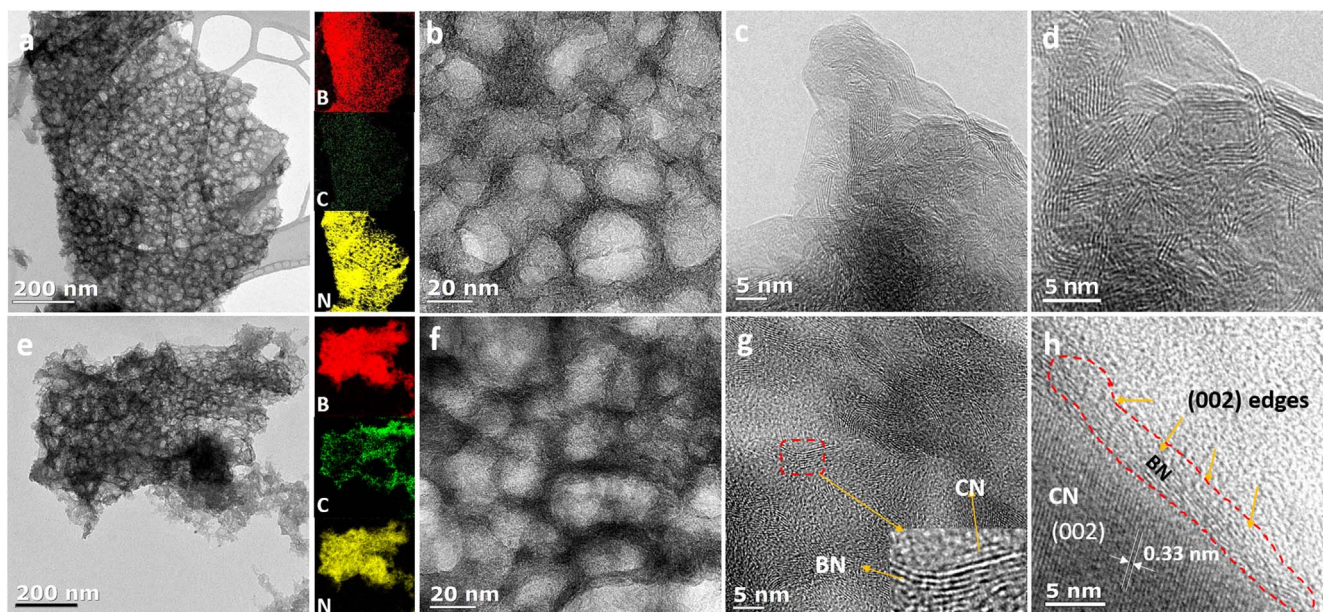


Fig. 2. HR-TEM images and EELS mapping data of *h*-BN (a–d) and CBN-6 (e–h).

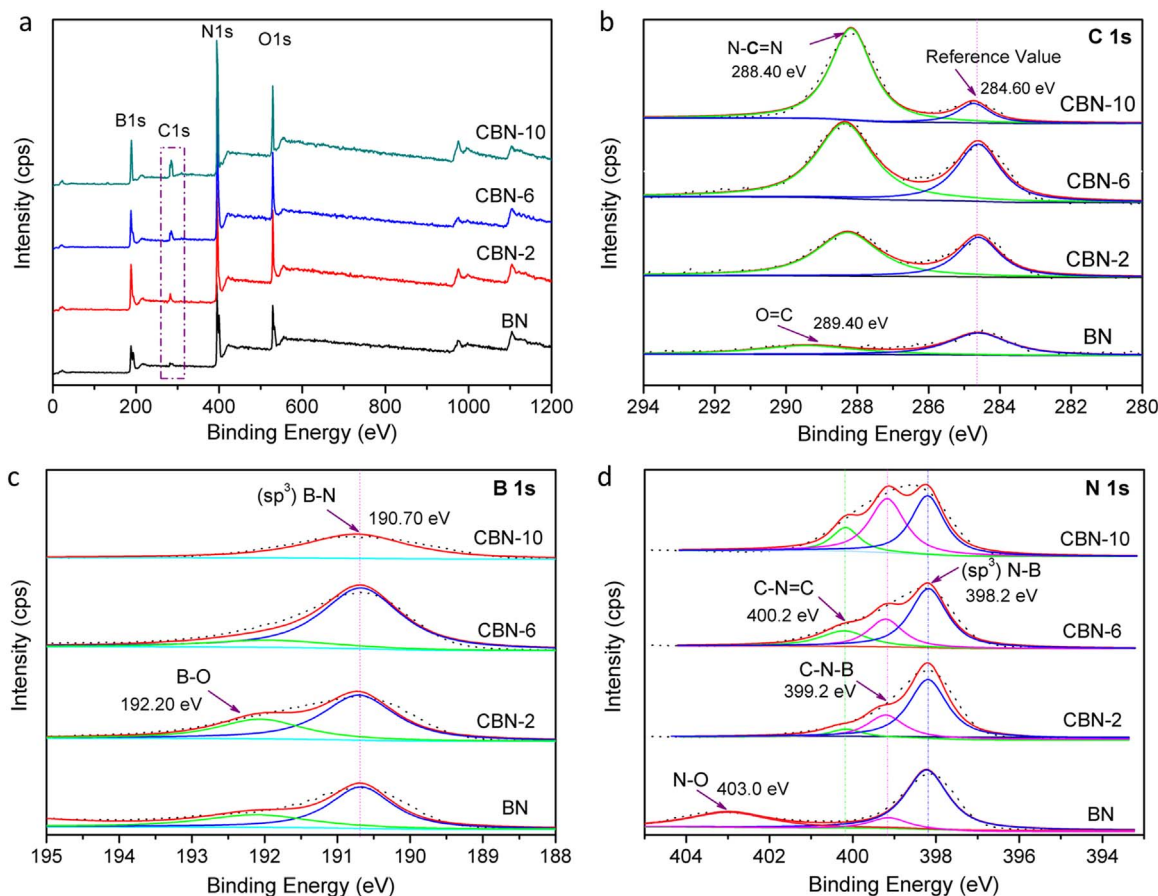


Fig. 3. (a) X-ray photoelectron spectra of *h*-BN and CBN-*x* samples, (b)–(d) showing the core level spectrum of C, B and N, respectively.

and pure CN (Fig. S5a), holes generated in *h*-BN should be transferred to CN phase at the heterojunction to enhance the charge separation efficiency. Therefore, increasing loading CN should enhance the overall charge separation efficiency until excessive loading of CN covers the active sites on *h*-BN with shielding light. We also compared the photocatalytic stability of CBN-6 with Pt-loaded *h*-BN (1 wt% Pt-BN), and found that CBN-6 is stable and more effective than Pt-BN for the photocatalytic H₂ production (see Fig. 4b). This indicates that CN loaded on *h*-BN creates an interfacial heterojunction that is very effective in separating charge pairs (electrons in *h*-BN and holes in CN). The subsequent electron transfer to the defect sites on *h*-BN surface or the (002) edge sites, may facilitate the evolution of H₂ (as illustrated in Fig. S5b). Fig. 4c compares the apparent quantum yields (AQY) of pure CN, *h*-BN and CBN-6 for H₂ production as a function of the wavelength. AQY of CBN-6 was calculated to be 0.33% at 305 nm, while that of *h*-BN and pure CN was 0.13% and 0.03%, respectively.

2.2.2. Photocatalytic H₂O₂ production

As another photocatalytic activity test, the production of H₂O₂ via O₂ reduction was measured by DPD method using a UV–Visible spectrophotometer. H₂O₂ has been frequently employed as an auxiliary oxidant in photocatalytic oxidation systems and in-situ production of H₂O₂ would be an alternative conversion reaction of solar utilization. Unlike the case of photocatalytic production of H₂, the production of H₂O₂ rapidly reached a saturation because the generated H₂O₂ can be immediately decomposed on the catalyst surface [36,37]. Kinetic analysis was carried out according to the equation of $[H_2O_2] = \frac{k_f}{k_d} \{1 - e^{-k_d t}\}$ where k_f and k_d are the formation and decomposition rate constant, respectively [37]. It is assumed that the formation rate is governed by zero-order kinetics because of continuous O₂ purging condition while the decomposition rate follows the first-order kinetics. Time dependent

UV–visible absorption spectral changes (after adding DPD reagent) during the photocatalytic H₂O₂ production in the suspension of CBN-4 and CBN-8 are shown in Fig. S6. And the Fig. 5a and b show the photocatalytic production and decomposition time profiles of H₂O₂. Fig. 5c compares the fitted values of k_d and k_f for Pt-BN, BN, CN and CBN-*x* samples. The photo-stationary concentration level of H₂O₂ is inversely proportional to k_d . The kinetic analysis clearly indicates that the overall photocatalytic production of H₂O₂ depended on both the formation and decomposition rate. The general trend is that the photocatalytic production of H₂O₂ increased with increasing the urea loading and the photocatalytic decomposition of H₂O₂ is more retarded at higher urea loading. Overall, CN exhibited the highest activity for H₂O₂ production and the lowest activity for H₂O₂ decomposition, which indicates that the CN phase is the main active site for H₂O₂ generation and the role of *h*-BN phase is insignificant in this case. And the CN loaded on the BN surface takes the important role in H₂O₂ generation in CN/BN hybrid system (as illustrated in Fig. S5b). Although the presence of *h*-BN is critical for the production of H₂, it is not essential for H₂O₂ production. The catalytic nature of *h*-BN is selective depending on the kind of electron acceptors (H₂O vs. O₂). The addition of Pt on *h*-BN enhanced the overall production of H₂O₂ but it also markedly accelerated the decomposition of H₂O₂. This makes Pt-BN an inefficient photocatalyst for H₂O₂ production whereas it is a fairly active photocatalyst for H₂ production. This is because Pt is a highly active catalyst for the decomposition of H₂O₂ despite its positive role of accelerating the forward reaction of O₂ reduction [37].

The photocatalytic oxidation (PCO) activities of the catalyst samples were also tested with using the degradation of 4-chlorophenol (4-CP) as a probe reaction (see Fig. S7). *h*-BN and all CBN-*x* samples exhibited similar activities for 4-CP degradation while CN showed markedly lower activity. This is because the main PCO activity is determined by

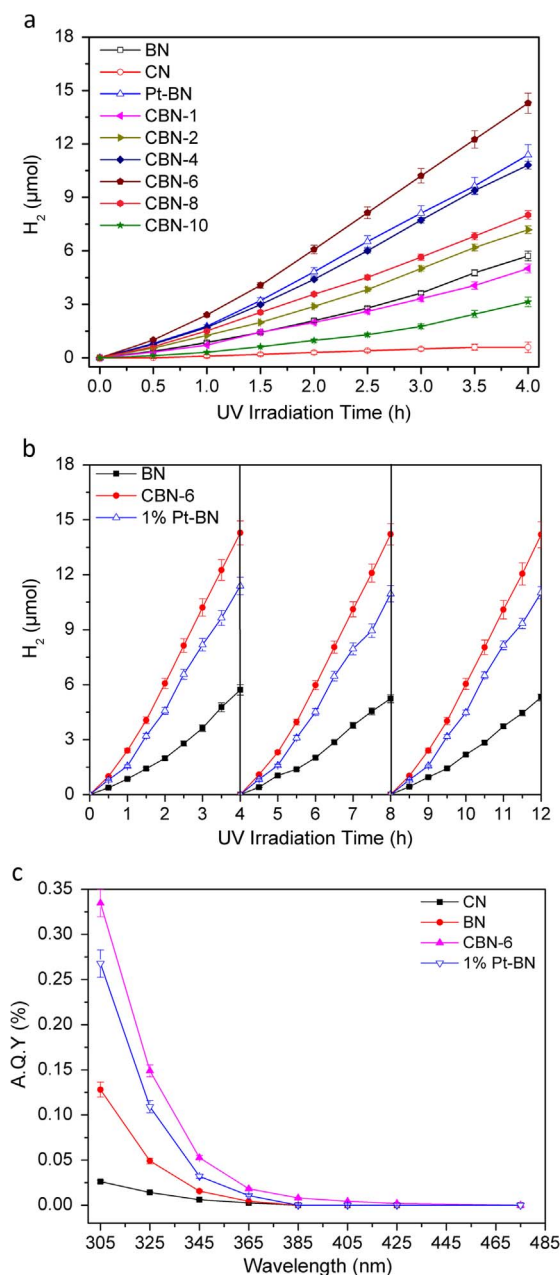


Fig. 4. (a) Time profiles of photocatalytic H₂ production in the presence of BN, CN or CBN-*x* samples. (b) Repeated cycles of H₂ production with BN, Pt-BN and CBN-6. Experimental conditions: 300-W Xe lamp ($\lambda > 305$ nm); [catalyst] = 0.5 g/L; [Methanol] = 10 vol%; pH = 3.0; initially Ar-saturated; a 55-mL Pyrex glass reactor. (c) Wavelength-dependent apparent quantum yield (AQY) of H₂ production with CN, BN, and CBN-6 samples. Experimental conditions: light filtered by a monochromator; [catalyst] = 0.5 g/L; [Methanol] = 10 vol%; pH = 3.0; initially Ar-saturated; a 35-mL glass reactor with a Pyrex window.

the oxidation potential of *h*-BN valance band (VB) edge level and CN VB potential is much less positive. Therefore the heterojunction created at the interface of *h*-BN and CN makes the VB holes transferred to the CN phase with sacrificing their oxidation potential. The CBN-*x* samples do not seem to have any merits for PCO reactions.

2.3. Charges' separation and band structures of the hybrid photocatalysts

An important parameter for efficient photocatalysis is a rapid separation of photogenerated electron-hole pairs. To investigate the effects of hybridization of CN and *h*-BN on the charge separation and the

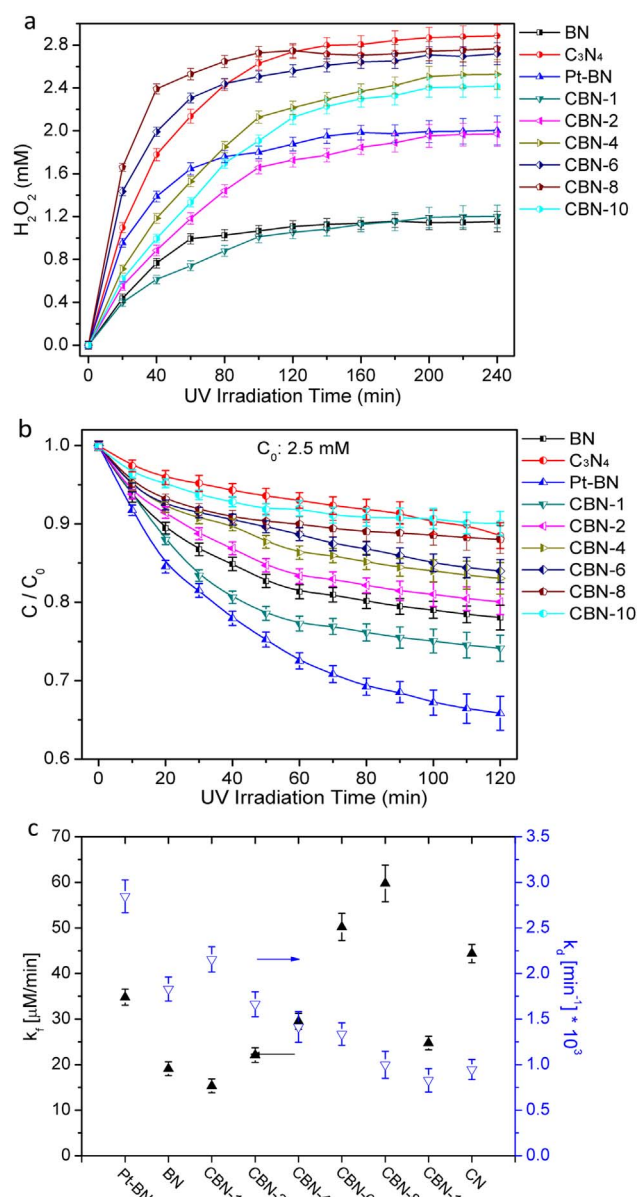


Fig. 5. (a) Time profiles of photocatalytic formation of H₂O₂; Experimental conditions: 300-W Xe lamp ($\lambda > 305$ nm); [catalyst] = 0.5 g/L; [Methanol] = 5 vol%; pH = 3.0; O₂-equilibrated; a 55-mL Pyrex glass reactor. (b) Photocatalytic decomposition of H₂O₂ (C₀ = 2.5 mM) under O₂-equilibrated conditions in presence of BN, CN or CBN-*x* samples; Experimental conditions: 300-W Xe lamp ($\lambda > 305$ nm); [catalyst] = 0.5 g/L; pH = 3.0; O₂-equilibrated; a 55-mL Pyrex glass reactor. (c) Formation rate constants (k_f, black filled symbol) and decomposition rate constants (k_d, blue opened symbol) for H₂O₂ in the presence of BN, CN and CBN-*x* samples.

subsequent interfacial charge transfer, the photocurrent was collected on a Pt electrode immersed in the irradiated catalyst suspension in the presence of Fe³⁺/Fe²⁺ redox couple serving as an electron shuttle (Fe³⁺ + e_{CB}⁻ → Fe²⁺; Fe²⁺ → Fe³⁺ + e⁻) [36,38–40]. Figs. 6a and S8 compares the time profiles of Fe³⁺-mediated photocurrent generation in various catalyst suspension. Compared with pure *h*-BN and CN, CBN-*x* samples exhibited enhanced photocurrent generation. The loading of Pt on *h*-BN also greatly enhanced the photocurrent. This implies that the charge pair separation in *h*-BN particle is facilitated in the presence of either CN layers or Pt nanoparticles on *h*-BN. That is, the roles of CN layers and Pt should be similar in enhancing the charge separation efficiency. The highest photocurrent generation efficiency obtained with CBN-6 is consistent with its highest photocatalytic H₂ production activity (see Fig. 4a). It confirms that the photo-induced electron transfer

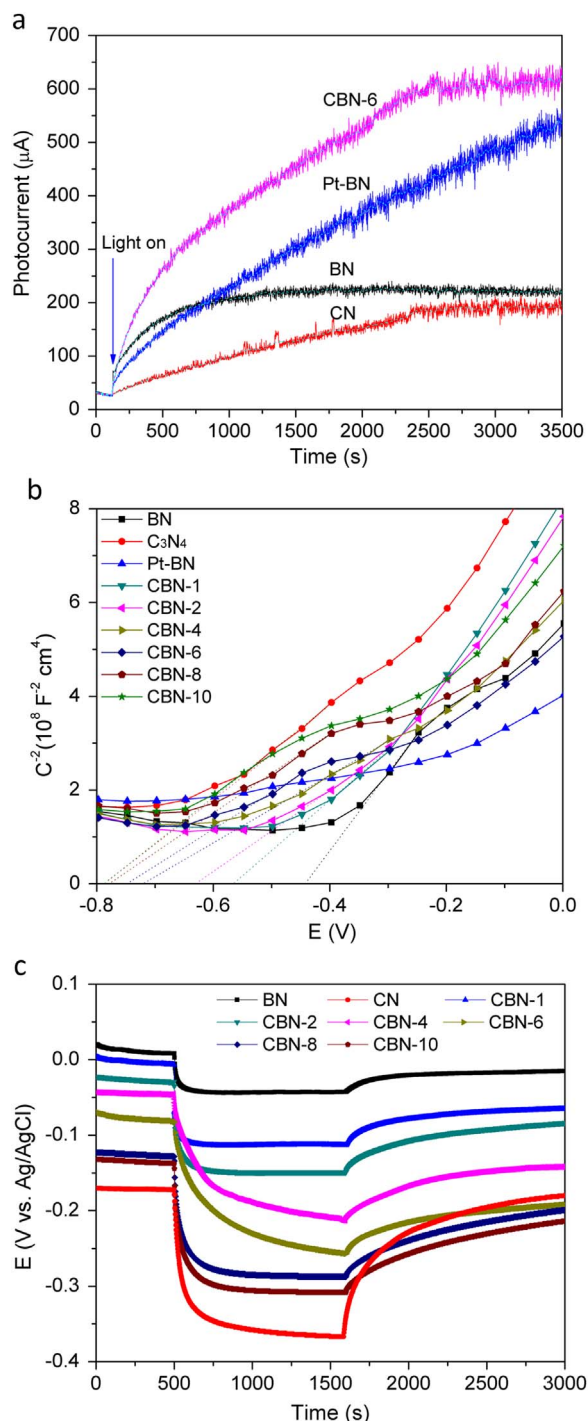


Fig. 6. (a) Time-dependent profiles of Fe^{3+} -mediated photocurrent in various photocatalysts suspensions under UV light ($\lambda > 305$ nm). Experimental conditions: [catalyst] = 1 g/L, $[\text{Fe}^{3+}] = 0.5$ mM, $[\text{NaClO}_4] = 0.1$ M, [Methanol] = 5 vol%, pH = 1.8, Pt electrode held at + 0.7 V (vs. Ag/AgCl), and continuously Ar-purged. (b) Mott-Schottky curves of BN, CN or CBN-x electrodes collected at a frequency of 1 kHz in the dark. Experimental conditions: $[\text{NaClO}_4] = 0.2$ M, pH = 3.0, electrode area of 4 cm^2 , and continuously Ar-purged. (c) Open circuit photo-potential (E_{ph}) measurement of BN, CN or CBN-x electrodes. Experimental conditions: $[\text{NaClO}_4] = 0.2$ M, pH = 3.0, electrode area of 4 cm^2 , $\lambda > 305$ nm, and continuously Ar-purged.

occurring on the suspended CBN-6 particles is clearly facilitated in the presence of CN/BN heterojunction [41].

To understand the effect of band structure on the photocatalytic activity, it is required to determine the band energy levels of each sample. It is usually assumed that the gap between the quasi-Fermi level

under illumination (nE_F^*) and the bottom edge of the conduction band (E_c) is negligible for n-type semiconductors, thus the measurement of nE_F^* is an approximate estimation of E_c [42]. The Fermi level is fixed at equilibrium in dark with the respect to the flat band (E_{fb}) and conduction band (E_c); the difference ($E_F - E_{\text{fb}}$) between ($E_c - E_F$) is determined by the doping or hybridizing density. ΔE_{fb} represents the energy of the photogenerated electrons under illumination [43]. E_{fb} becomes more negative with respect to the standard potential as E_F does, thus the driving force or overpotential for reduction reactions increases [44]. Under the photostationary condition, the flat band shift (ΔE_{fb}) in potential under illumination ($E_{\text{ph}} - E_0$) is equivalent to the change in the E_F due to the promotion of electrons to the conduction band, and it reaches a maximum value at nE_F^* [42,44]. The nE_F^* can be determined by measuring E_{fb} according to the Mott-Schottky analysis and the ΔE_{fb} according to the stationary open-circuit potential in dark (E_0) or under illumination (E_{ph}). Loading CN on *h*-BN nanosheets favors the facile injection of photogenerated electrons from the CN's CB to BN's CB. As shown in Fig. 6b, the flat band potential of BN, CN and CBN-x was determined to be - 0.44, - 0.79, - 0.44, - 0.56, - 0.63, - 0.72, - 0.75, - 0.77 and - 0.78 V (vs. Ag/AgCl), respectively. As observed from Fig. 6c, the stationary open-circuit potential in the dark (E_0), which is the equilibrium potential of an electrode in contact with the electrolyte solution, immediately shifted to more negative values under illumination and reached the photosteady-state (E_{ph}) with time, which confirms the n-type character of the semiconductor materials. Based on these values of flat band potentials and the optical band gap energies summarized in Table 2, we constructed the potential energy diagram for the CBN-x hybrid photocatalysts in Scheme 1. The E_g of CBN-x samples is reduced from 3.84 eV (CBN-1) to 2.67 eV (CBN-10), which was estimated from UV-Visible spectra. The E_c gradually shifts from - 0.30 V (CBN-1) to - 0.58 V (CBN-10), while the E_v gradually shifts upwards from 3.54 V (CBN-1) to 2.09 V (CBN-10). This gradual band level change illustrates how the hybrid photocatalysts can precisely tune the band structures with controlling the loading of CN. In addition, the open circuit potential (OCP) decay of the CBN-6 electrode, which was monitored immediately after turning off the UV light, is markedly slower than other electrodes (see Fig. S9). This indicates a slowest recombination rate in the CBN-6 electrode. It indicates that CN loaded on the surface of *h*-BN created an interfacial region in which the charge pairs are efficiently separated. To further confirm the enhanced charge transfer rate of the CBN-6 electrode, electrochemical impedance spectroscopy (EIS) measurements were also carried out. As shown in

Table 2
Electronic properties of BN, CN and CBN-x electrodes.

Samples	E_g^a (eV)	E_0^b (vs. Ag/AgCl) (mV)	E_{ph}^c (vs. Ag/AgCl) (mV)	$E_{\text{ph}} - E_0$ (vs. Ag/AgCl) (mV)	E_{fb}^d (vs. Ag/AgCl) (mV)	E_c^e (vs. NHE) (mV)	E_v^f (V)
BN	3.98	4	- 32	- 36	- 443	- 105	3.85
CBN-1	3.84	- 4	- 112	- 108	- 564	- 298	3.54
CBN-2	3.68	- 30	- 150	- 120	- 626	- 372	3.31
CBN-4	3.47	- 46	- 211	- 165	- 718	- 509	2.96
CBN-6	3.13	- 82	- 257	- 175	- 746	- 547	2.58
CBN-8	2.86	- 126	- 287	- 161	- 774	- 561	2.30
CBN-10	2.67	- 137	- 308	- 171	- 784	- 581	2.09
CN	2.76	- 173	- 365	- 192	- 786	- 604	2.16

^a Calculated band gap E_g from UV-Visible spectra.

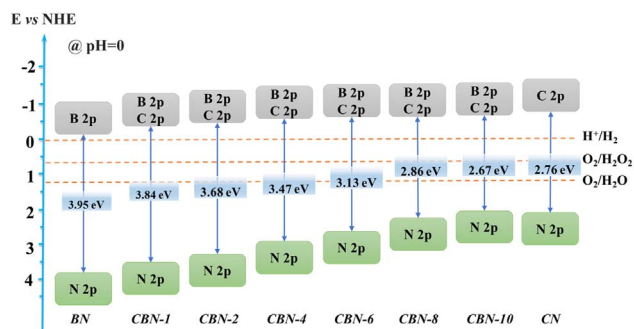
^b Measured open circuit potential E_0 at pH = 3.0 in the dark after equilibrium.

^c Measured open circuit photo-potential E_{ph} at pH = 3.0 under illumination after equilibrium.

^d Measured flat band potential E_{fb} from Mott-Schottky plots collected at a frequency of 1 kHz in the dark.

^e Calculated conduction band potential at pH = 0 (vs. NHE), converting the obtained potential (vs. Ag/AgCl) to the potential against NHE according to $E_c \approx nE_F^* = E_{\text{fb}} + (E_{\text{ph}} - E_0) + E_{\text{vs. Ag/AgCl}}^0 + 0.059 \text{ pH}$, $E_{\text{vs. Ag/AgCl}}^0 = 0.197$ V.

^f Calculated valence band potential according to $E_v = E_g + E_c$.



Scheme 1. Determined band energy levels of CBN-x electrodes, in comparison with pure *h*-BN and CN electrodes. The standard reduction potentials for H^+/H_2 , O_2/H_2O_2 and O_2/H_2O couples are shown as a reference.

Fig. S10, the arc size of the CBN-6 sample is the smallest among all the samples. A smaller arc size in an EIS Nyquist plot indicates a smaller charge-transfer resistance on the electrode interface, which also supports the more efficient charge transfer in the CBN-6 electrode [45].

2.4. Calculation of density of states

The activity of photocatalysts is related significantly to the bandgap and the position of CB and VB of the material. Finally, we investigated the probable electronic structure and ion-decomposed electronic density of states by means of comprehensive density functional theory (DFT) computations based on first principles calculations. In **Fig. 7**, we show the schematic structures and charge distribution of *h*-BN, CN, C-BN and CN/BN samples. The green, blue and gray spheres represent the B, N, C atoms, respectively. **Fig. 8** compare the calculated band structures of these samples. From DFT calculations, pure *h*-BN possesses an indirect band gap of 4.56 eV (**Figs. 7a** and **8a**), consistent with the previous theoretical values [46]. This is about 0.59 eV smaller than the experimental value, due to the well-known limitation of the DFT within GGA method [10,47]. The electronic structure and ion-decomposed electronic density of states of CN were also shown in **Figs. 7b** and **8b** for comparison. The CB minimum and VB maximum are all composed of C 2p and N 2p. The total density of states (DOS) shows that the value of E_g (bandgap between the top of VB and the bottom of CB) is ca. 1.70 eV for CN [48]. Our computations revealed that C-doping into *h*-BN nanosheets can cause high spin density and charge density and reduce the bandgap as shown in **Figs. 7c** and **8c**, the band gap of C-doped *h*-BN is significantly reduced from 4.56 to 2.95 eV. Different from that of pure *h*-BN (**Fig. 7a**), the partial density of states indicates that the VB and CB edges of C-doped *h*-BN are mainly composed of the C 2p orbitals (**Fig. 8c**). Calculation results on the CN/BN heterostructures are shown in **Figs. 7d** and **8d**. Similar results of the band structure were obtained, which shows a smaller band gap of 1.70 eV as a result of the CN loading on *h*-BN (also here is about 1.00 eV smaller than the experimental value of 2.7 eV for CN as shown in **Fig. 1b** and **Table 1**) [48,49].

3. Conclusion

In summary, we introduced a new kind of 2D heterojunction created by loading CN on *h*-BN nanosheets. Although *h*-BN has a large bandgap (~ 4 eV), it has a catalytic activity for H_2 production and the hybrid CBN-x samples exhibited H_2 production activity without the need of noble metal cocatalysts. The optimal hybrid of CBN-6 was even more reactive than Pt-BN for the photocatalytic production of H_2 whereas pure CN alone exhibited very lower activity for H_2 production. Photocatalytic H_2O_2 production activities of hybrid CBN-x samples were also proven to be enhanced from that of *h*-BN. In such metal-free hybrid photocatalysts, CN loaded on the surface of *h*-BN created an interfacial region where the photogenerated charge pairs are efficiently

separated into different parts (electrons in *h*-BN and holes in CN) as a result of the band edge mismatch. Although the reduction potential of the photogenerated electrons are reduced upon their transfer from CN's CB to BN's CB, holes are transferred into the CN phase to achieve better charge separation and prolong the lifetime of the electrons, which enhances the overall efficiency of photocatalysis as shown in **Figs. 4** and **5**. The present hybrid photocatalyst of CN/BN provides a new example of 2D heterostructure system with tunable photo(electro)chemical properties, which can be employed as a new kind of solar conversion base material.

4. Experimental section

4.1. Synthesis of porous *h*-BN nanosheets

Boric acid (4 g) and urea (16 g) were mixed in 80 mL water to form a clear colorless solution at 80 °C for 4 h. After water was removed in a rotary evaporator, the mixed precursor solution was transferred into a quartz boat, which was transformed into gels after cooling to room temperature. Then the quartz boat was put into a horizontal tube furnace, and the sample was annealed to 900 °C for 5 h at a heating rate of 5 °C/min under nitrogen gas. White *h*-BN sample was obtained after washing with ethanol.

4.2. Direct growth of CN on porous *h*-BN nanosheets

Urea was used as a precursor of CN that was directly deposited on porous *h*-BN nanosheets. 0.2 g of the synthesized *h*-BN nanosheets was mixed with different amounts of urea (0.2 g, 0.4 g, 0.8 g, 1.2 g, 1.6 g, 2.0 g) in an agate mortar. And then the well-mixed powder was put into a 30-mL alumina crucible with a cover and then heated to 550 °C in a muffle furnace for 30 min at a heating rate of 15 °C/min. The resulted powder was collected for use after washing with water to remove B_2O_3 . The final samples were denoted as CBN-x, where x (1, 2, 4, 6, 8, 10) is the mass ratio of urea to BN in the CN growth process as shown in **Fig. S1**. Pure CN was also synthesized by heating urea at 550 °C for 30 min.

4.3. Characterization

X-ray diffraction (XRD; Rigaku, RINT 2000) was carried out in order to investigate the phase of each *h*-BN and CBN sample. The morphology and crystallography of the samples were examined using a field-emission scanning electron microscope (FE-SEM; JEOL, JSM-7401F) and a high-resolution transmission electron microscope (HR-TEM; JEOL, JEM-2200FS) with the electron energy-loss spectroscopy (EELS) analysis, which was carried out at National Institute for Nanomaterials Technology (NINT) in Pohang, Korea. X-ray photoelectron spectroscopy (XPS) spectra for surface analysis were collected using AXIS-NOVA (Kratos, Inc) with employing Al $K\alpha$ line (1486.6 eV) as the excitation source at Korea Basic Science Institute (KBSI). The shift in the binding energy due to the surface charging was corrected by using the C1s band at 284.6 eV as an internal standard. Nitrogen adsorption was performed with Micromeritics ASAP 2020 (USA) to determine the Brunauer-Emmett-Teller (BET) specific surface area of the as-synthesized products. UV-visible absorption spectra were recorded on a UV-visible spectrophotometer (Shimadzu UV-2600). Fourier transform infrared spectroscopy (FTIR) was recorded with pelletized samples on a Thermo Scientific Nicolet iS50 FT-IR spectrophotometer, equipped with an iS50 ATR accessory (Thermo Scientific, Madison, USA).

4.4. Photocatalytic activity tests

The photocatalytic activities of the as-synthesized samples were measured in an aqueous suspension in a pyrex reactor for H_2 and H_2O_2 production, where methanol was added as an electron donor. For the H_2 production experiments, 15 mg catalytic sample was dispersed in 27 mL

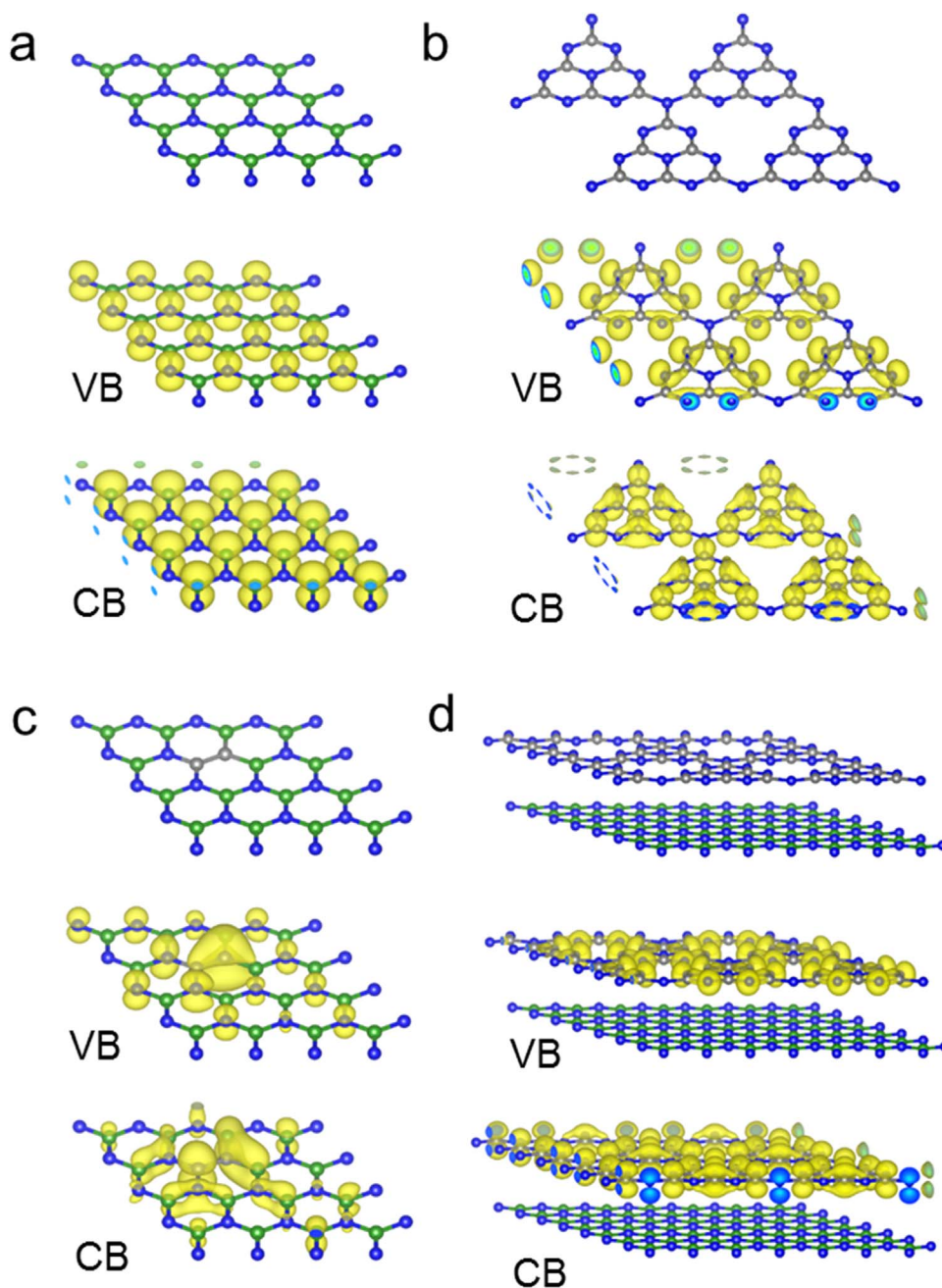


Fig. 7. The plane-wave DFT calculations of the electronic structure of *h*-BN (a), CN (b), C-doped *h*-BN (c) or CN/BN (d) with corresponding charge distribution of VB (the upper part) and CB (the lower part). The B atoms are represented by green spheres, N atoms by blue spheres, and C atoms by gray spheres.

distilled water under sonication for 3 min in an ultrasonic cleaning bath. The pH of the suspension was adjusted with concentrated HClO₄ after adding 3 mL methanol. The reactor was sealed with a rubber septum and purged with Ar gas for 30 min prior to irradiation to remove dissolved oxygen. A 300-W Xe arc lamp (Oriel) was used as the light source for the photocatalytic reactions. Light was passed through a 10-cm IR water filter and a UV-cutoff filter ($\lambda > 305$ nm), and then the filtered light was focused onto a 55.5 mL pyrex reactor. The photo-produced H₂ was sampled in the headspace of the sealed reactor and analyzed by using a gas chromatograph (GC, HP6890A) with a thermal conductivity detector and Ar as a carrier gas. The stability of photocatalytic H₂ production activity was measured by repeating the photocatalysis cycles in a pyrex reactor containing the same batch of catalyst, the catalyst suspension was purged with Ar gas for 30 min at the end of each irradiation cycle (4 h for each cycle).

The apparent quantum yields (AQY) for H₂ production defined by Eq. (1) were measured by using monochromatic irradiation filtered by a

Newport Oriel 77250 Monochromator. The incident monochromatic irradiation power was measured by a NOVA power monitor.

$$\text{A.Q.Y. [\%]} = \frac{\text{number of evolved H}_2 \text{ molecules} \times 2}{\text{number of incident photons}} \times 100 \quad (1)$$

The photocatalytic H₂O₂ production experiments were also conducted in aqueous photocatalyst suspension which was irradiated by a 300-W Xe arc lamp (the same irradiation condition for H₂ production experiments). 20 mg of catalytic sample was dispersed in water (36 mL) and 4 mL of methanol was added as an electron donor. After sonication for catalyst dispersion, the pH of the suspension was adjusted to pH 3.0 by HClO₄. The solution was continuously purged by O₂ gas while it was stirred for 30 min prior to irradiation. The H₂O₂ production was conducted in a pyrex reactor under continuous stirring and O₂ bubbling during the irradiation. The concentration of H₂O₂ was determined by the DPD colorimetric method, which is based on the horseradish peroxidase (Aldrich)-catalyzed reaction of H₂O₂ with N,N-diethyl-p-

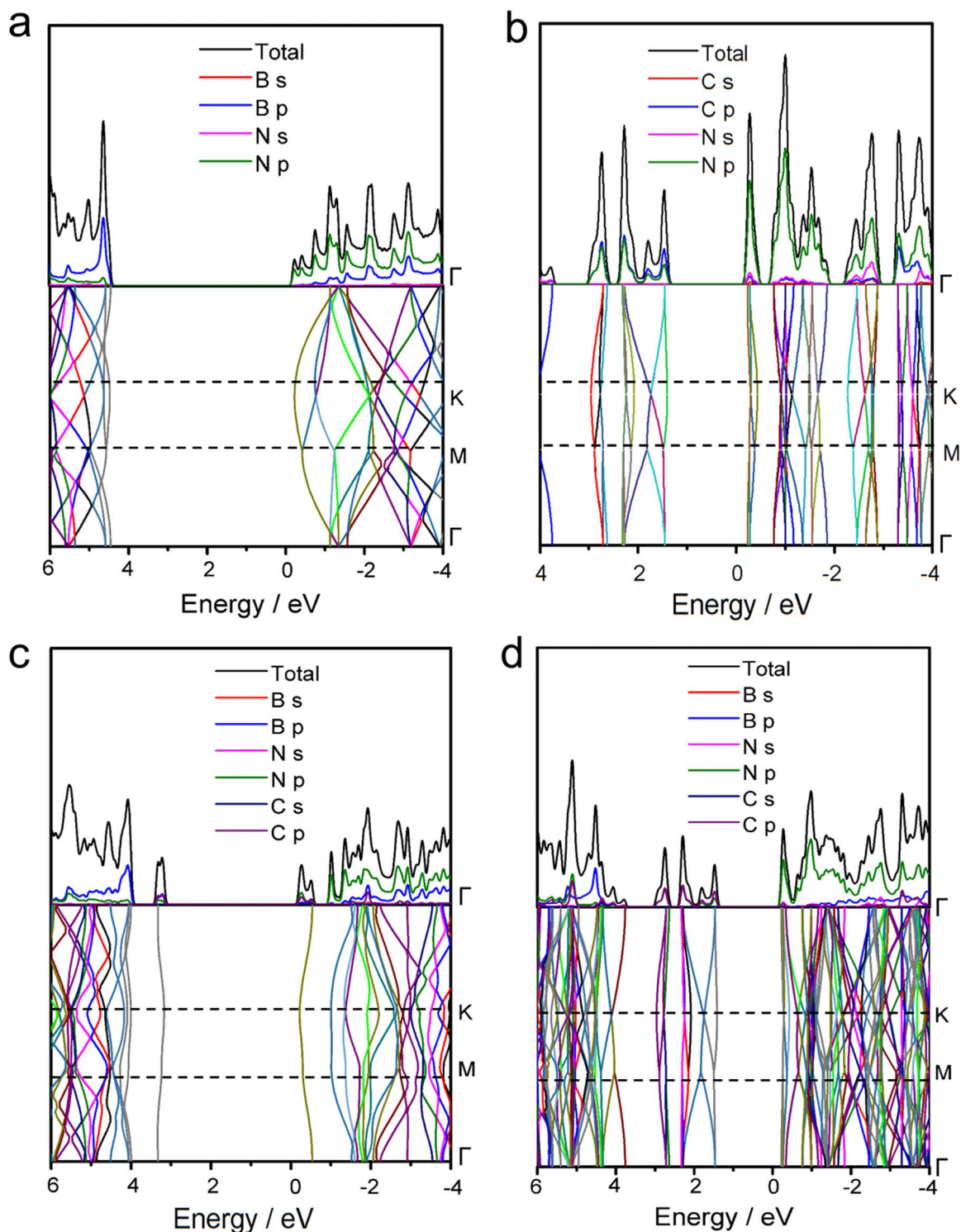


Fig. 8. Band structures and corresponding total and ion-decomposed electronic DOS of *h*-BN (a), CN (b), C-doped *h*-BN (c) or CN/BN (d).

phenylenediamine (DPD, 97%, Aldrich). The absorbance was measured at 551 nm using a UV–visible spectrophotometer. Prior to analysis, 1 mL of sample aliquots were collected by a syringe during the irradiation and the photocatalyst particles were removed by filtering through a 0.45 μm PTFE syringe filter (Millipore).

4.5. Photoelectrochemical measurements

Two types of photoelectrochemical (PEC) measurements (electrode

or slurry test) were carried out in a conventional three-electrode system connected to a potentiostat (Gamry, Reference 600). The slurry-type PEC tests were conducted in a suspension of catalyst using a Pt wire, a graphite rod, and a Ag/AgCl electrode as a working, a counter, and a reference electrode, respectively, under continuous stirring and Ar gas purging. The electrons generated on photocatalytic particles in suspension were collected on the Pt wire as the working electrode biased at + 0.6 V (vs. Ag/AgCl) through electron shuttles (using a reversible redox couple of $\text{Fe}^{3+}/\text{Fe}^{2+}$) under light irradiation. The same 300-W Xe

arc lamp (Oriel) was used as a light source as in the photocatalysis experiments.

The electrode-type PEC tests were also carried out with using a photo-electrode (FTO glass coated with samples), a coiled Pt wire, and a Ag/AgCl electrode as a working, a counter, and a reference electrode, respectively, which were immersed in an aqueous electrolyte solution consisting of NaClO₄ (0.2 M) and methanol (10 vol%) at pH 3.0, and continuously purged with Ar gas during the measurement. The photo-electrodes were prepared using a doctor blade method. The catalyst paste in a 5 wt% poly(vinylidene fluoride) (PVDF)/N-methyl-2-pyrrolidone (NMP) solution was spread on an FTO glass (Pilkington, TEC8) and then dried at 120 °C overnight. The obtained photoelectrodes have an average active area of about 4 cm². Electrochemical impedance spectroscopy (EIS) was conducted with a constant DC voltage at + 0.6 V (vs. Ag/AgCl), a voltage amplitude of 10 mV, and the frequency range of 0.1–10⁶ Hz.

4.6. Theoretical calculation

The plane-wave DFT calculations were carried out by using the Vienna ab initio simulation package with the gradient-corrected PW91 exchange-correction function. For valence electrons, a plane-wave basis set was adopted with an energy cutoff of 400 eV and the ionic cores were described with the projector augmented-wave method. The optimized lattice parameter for a *h*-BN monolayer was calculated to be 2.49 Å, which is in good agreement with the experimental result (2.54 Å). A supercell *h*-BN shown in Fig. 7a is constructed as a substrate. For the optimization of all the relaxation atoms, Monkhorst–Pack k-point grids were used to sample the Brillouin zone, which were tested to be converged, whereas for electronic properties calculations, the Brillouin zone was sampled by k-points. In addition, to avoid the inter-layer interactions, a vacuum spacing in the *z* direction was set to be 14 Å. The supercell CN shown in Fig. 7b is constructed as a substrate. At the beginning of the urea loading, C atoms might be incorporated into *h*-BN lattice to form C-doped *h*-BN with creating a small number of C–B or C–N bonds in this compound as shown in Fig. 7c. With further increasing the urea loading, the C and N from urea will reform to a lower free energy compound (CN) on *h*-BN surface as shown in Fig. 7d. Consequently, the hybrid systems will be domain-segregated into two different phases, one with CN-enriched domain and the other with BN-enriched domain as shown in Fig. 7d, to gain thermodynamic stability [50]. As result, we build a new 2D heterostructure of the hybridization of *h*-BN and CN (CN/*h*-BN), which was supported by the present experimental data.

Acknowledgements

This work was financially supported by Basic Science Research Program (NRF-2017R1A2B2008952) and KCAP (Sogang Univ.) (No. 2009-0093880), which were funded by the Korea Government (MSIP) through the National Research Foundation (NRF). Also Prof. Wang thanks the National Natural Science Foundation of China (21425309 and 21761132002) for supporting this work.

Appendix A. Supplementary material

Supplementary data associated with this article can be found in the online version at <http://dx.doi.org/10.1016/j.nanoen.2017.10.043>.

References

- [1] Y. Zhang, Y.W. Tan, H.L. Stormer, P. Kim, Nature 438 (2005) 201–204.
- [2] C. Lee, X. Wei, J.W. Kysar, J. Hone, Science 321 (2008) 385–388.
- [3] X. She, J. Wu, J. Zhong, H. Xu, Y. Yang, R. Vajtai, J. Lou, Y. Liu, D. Du, H. Li, P.M. Ajayan, Nano Energy 27 (2016) 138–146.
- [4] F. Koppens, T. Mueller, P. Avouris, A. Ferrari, M. Vitiello, M. Polini, Nat. Nanotechnol. 9 (2014) 780–793.
- [5] D. Deng, K.S. Novoselov, Q. Fu, N. Zheng, Z. Tian, X. Bao, Nat. Nanotechnol. 11 (2016) 218–230.
- [6] X. Wang, K. Maeda, A. Thomas, K. Takanabe, G. Xin, J.M. Carlsson, K. Domen, M. Antonietti, Nat. Mater. 8 (2009) 76–80.
- [7] F. Ma, Y. Wu, Y. Shao, Y. Zhong, J. Lv, X. Hao, Nano Energy 27 (2016) 466–474.
- [8] X. Wang, S. Blechert, M. Antonietti, ACS Catal. 2 (2012) 1596–1606.
- [9] Q. Han, B. Wang, Y. Zhao, C. Hu, L. Qu, Angew. Chem. Int. Ed. 54 (2015) 11433–11437.
- [10] C. Huang, C. Chen, M. Zhang, L. Lin, X. Ye, S. Lin, M. Antonietti, X. Wang, Nat. Commun. 6 (2015) 7698.
- [11] J. Grant, C. Carrero, F. Goeltl, J. Venegas, P. Mueller, S. Burt, S. Specht, W. McDermott, A. Chiericato, I. Hermans, Science 354 (2016) 1570–1573.
- [12] Z. He, W. Que, Appl. Mater. Today 3 (2016) 23–56.
- [13] S. Yang, Y. Gong, J. Zhang, L. Zhan, L. Ma, Z. Fang, R. Vajtai, X. Wang, P.M. Ajayan, Adv. Mater. 25 (2013) 2452–2456.
- [14] W. Tu, Y. Zhou, Q. Liu, Z. Tian, J. Gao, X. Chen, H. Zhang, J. Liu, Z. Zou, Adv. Funct. Mater. 22 (2012) 1215–1221.
- [15] Y. Wang, X. Wang, M. Antonietti, Angew. Chem. Int. Ed. 51 (2012) 68–89.
- [16] J. Duan, S. Chen, M. Jaroniec, S.Z. Qiao, ACS Nano 9 (2015) 931–940.
- [17] A.K. Geim, I.V. Grigorieva, Nature 499 (2013) 419–425.
- [18] W.J. Ong, L.L. Tan, S.P. Chai, S.T. Yong, A.R. Mohamed, Nano Energy 13 (2015) 757–770.
- [19] Z.S. Wu, Y. Zheng, S. Zheng, S. Wang, C. Sun, K. Parvez, T. Ikeda, X. Bao, K. Mullen, X. Feng, Adv. Mater. 29 (2017) 1602960.
- [20] Q. Fu, X. Bao, Chem. Soc. Rev. 46 (2017) 1842–1874.
- [21] W. Lei, D. Portehault, D. Liu, S. Qin, Y. Chen, Nat. Commun. 4 (2013) 1777.
- [22] Z. Zhang, Y. Liu, Y. Yang, B.I. Yakobson, Nano Lett. 16 (2016) 1398–1403.
- [23] C. Zhi, Y. Bando, C. Tang, H. Kuwahara, D. Golberg, Adv. Mater. 21 (2009) 2889–2893.
- [24] M. López-Suárez, G. Abadal, L. Gammaitoni, R. Rurali, Nano Energy 15 (2015) 329–334.
- [25] C. Gautam, C.S. Tiwary, S. Jose, G. Bruneto, S. Ozden, S. Vinod, P. Raghavan, S. Biradar, D.S. Galvao, P.M. Ajayan, ACS Nano 9 (2015) 12088–12095.
- [26] H. Si, G. Lian, J. Wang, L. Li, Q. Wang, D. Cui, C.-P. Wong, ACS Appl. Mater. Interfaces 8 (2016) 1578–1582.
- [27] M. Wang, M. Li, L. Xu, L. Wang, Z. Ju, G. Li, Y. Qian, Catal. Sci. Technol. 1 (2011) 1159–1165.
- [28] S.-K. Kim, H. Cho, M.J. Kim, H.-J. Lee, J.-h. Park, Y.-B. Lee, H.C. Kim, C.W. Yoon, S.W. Nam, S.O. Kang, J. Mater. Chem. A 1 (2013) 1976–1981.
- [29] Q. Weng, Y. Ide, X. Wang, X. Wang, C. Zhang, X. Jiang, Y. Xue, P. Dai, K. Komaguchi, Y. Bando, D. Golberg, Nano Energy 16 (2015) 19–27.
- [30] A. Thomas, A. Fischer, F. Goettmann, M. Antonietti, J.O. Müller, R. Schlögl, J.M. Carlsson, J. Mater. Chem. 18 (2008) 4893–4908.
- [31] Y. Zheng, J. Liu, J. Liang, M. Jaroniec, S.Z. Qiao, Energy Environ. Sci. 5 (2012) 6717–6731.
- [32] J. Liu, Y. Liu, N. Liu, Y. Han, X. Zhang, H. Huang, Y. Lifshitz, S.-T. Lee, J. Zhong, Z. Kang, Science 347 (2015) 970–974.
- [33] Y. Hou, Z. Wen, S. Cui, X. Guo, J. Chen, Adv. Mater. 25 (2013) 6291–6297.
- [34] W. Wang, J.C. Yu, D. Xia, P.K. Wong, Y. Li, Environ. Sci. Technol. 47 (2013) 8724–8732.
- [35] D.J. Martin, K. Qiu, S.A. Shevlin, A.D. Handoko, X. Chen, Z. Guo, J. Tang, Angew. Chem. Int. Ed. 53 (2014) 9240–9245.
- [36] H. Kim, O.S. Kwon, S. Kim, W. Choi, J.-H. Kim, Energy Environ. Sci. 9 (2016) 1063–1073.
- [37] G. Moon, W. Kim, A.D. Bokare, N. Sung, W. Choi, Energy Environ. Sci. 7 (2014) 4023–4028.
- [38] S. Hamid, I. Ivanova, T.H. Jeon, R. Dillert, W. Choi, D.W. Bahnemann, J. Catal. 349 (2017) 128–135.
- [39] W.W. Dunn, Y. Aikawa, A.J. Bard, J. Electrochem. Soc. 128 (1981) 222–224.
- [40] H. Kim, H. Kim, S. Weon, G. Moon, J.H. Kim, W. Choi, ACS Catal. (2016) 8350–8360.
- [41] Y.J. Cho, H. Kim, S. Lee, W. Choi, J. Catal. 330 (2015) 387–395.
- [42] G. Zhang, D. Monllor-Satoca, W. Choi, Catal. Sci. Technol. 3 (2013) 1790–1797.
- [43] M.D. Ward, J.R. White, A.J. Bard, J. Am. Chem. Soc. 105 (1983) 27–31.
- [44] X. Li, J. Yu, J. Low, Y. Fang, J. Xiao, X. Chen, J. Mater. Chem. A 3 (2015) 2485–2534.
- [45] E.H. Kong, J. Lim, J.H. Lee, W. Choi, H.M. Jang, Appl. Catal. B: Environ. 176 (2015) 76–82.
- [46] J. Zhao, Z. Chen, J. Phys. Chem. C 119 (2015) 26348–26354.
- [47] X. Li, J. Zhao, J. Yang, Sci. Rep. 3 (2013) 1858.
- [48] Y. Zheng, Y. Jiao, Y. Zhu, L.H. Li, Y. Han, Y. Chen, A. Du, M. Jaroniec, S.Z. Qiao, Nat. Commun. 5 (2014) 3783.
- [49] J. Wang, Z. Guan, J. Huang, Q. Li, J. Yang, J. Mater. Chem. A 2 (2014) 7960–7966.
- [50] A. Hashmi, J. Hong, Sci. Rep. 4 (2014) 4374.



Zuoli He received B.S. in materials science at Shandong Polytechnic University in 2008, M.S. in materials science and engineering at Shaanxi University of Science and Technology in 2011, and Ph.D. in Electronic Science and Technology at Xi'an Jiaotong University in 2015. He spent one year at University of Utah as a visiting researcher (2013–2014) and two years in Prof. Wonyong Choi's group at Division of Environmental Science and Engineering, POSTECH as a postdoctoral researcher (2015–2017). He is currently a postdoctoral researcher in Korea Institute of Materials Science (KIMS). His current research interests focus on nanostructured semiconductor materials for photocatalysis and photochemistry for solar energy conversion.



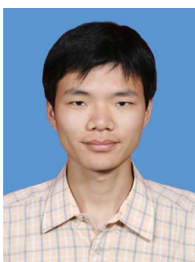
Sen Lin received B.S. in chemistry from Sichuan University in 2006 and Ph.D. in physical chemistry from Nanjing University in 2011. He is currently an associate professor in State Key Laboratory of Photocatalysis on Energy and Environment, College of Chemistry, Fuzhou University, P. R. China. His research is focused on the theoretical studies in reaction mechanism of heterogeneous catalysis.



Chuhyung Kim received B.S. in Chemical Engineering at Tsinghua University (Beijing, China) in 2014 and currently pursuing a Ph.D. study under the supervision of Prof. Wonyong Choi at POSTECH (Pohang, Korea). His research interests include photocatalytic hydrogen peroxide production and nanomaterials for environmental oxidation processes.



Xinchun Wang is currently the director of the State Key Laboratory of Photocatalysis on Energy and Environment, and the dean of college of chemistry in Fuzhou University. He obtained his B.S. and M.S. in Fuzhou University, and went to The Chinese University of Hong Kong to pursue his Ph.D. study. In 2006, he moved to Tokyo University as a JSPS post-doctor, then he went to Max Planck Institute of Colloids and Interfaces, Germany, as Alexander von Humboldt fellow, and was promoted as a Group Leader during 2008–2012. He started his professorship in Fuzhou University at 2005. His research interests cover catalysis and photocatalysis, and in this research field he published more than 190 peer-reviewed papers with H-index of 76.



Lihua Lin received B.S. in Physics at Harbin University in 2009, M.S. in Atomic and Molecular Physics at Anhui Normal University in 2013, and Ph.D. in Physical Chemistry at Fuzhou University in 2017. He is currently a Post-Doctor supervised by Prof. Xinchun Wang in State Key Laboratory of Photocatalysis on Energy and Environment, College of Chemistry, Fuzhou University, P. R. China. His research focuses on the utilization of solar energy and carbon nitride materials in photocatalytic water splitting.



Wonyong Choi received B.S. in engineering from Seoul National University in 1988, M.S. in chemistry from POSTECH in 1990, and Ph.D. in chemistry from California Institute of Technology in 1996. After postdoctoral research in atmospheric chemistry at Jet Propulsion Laboratory (1996–1998), he joined the faculty of POSTECH and was promoted to full professor in 2008. His research interests are mainly focused on semiconductor photocatalysis and photochemistry for solar energy conversion and environmental applications, advanced oxidation processes, and environmental chemistry. He has published over 260 papers in peer-reviewed journals, which have been cited over 29,000 times (H-index 71). He is serving as Associate Editor

of *Environmental Science & Technology* (ACS, 2017–).



Tae Hwa Jeon received B.S. in Physics and Energy Science at Kyungpook National University (KNU; Daegu, Korea) in 2010, M.S. in Physics and Energy Science, KNU in 2012 (advisor: Hyunwoong Park), and Ph.D. in Division of Environmental Science and Engineering, POSTECH (Pohang, Korea) in 2017 under the supervision of Prof. Wonyong Choi. He is interested in photoelectrochemical water oxidation.